ADVANCED OPTICAL MATERIALS
www.advopticalmat.de

Modified Zinc Magnesium Oxide for Optimal Charge-Injection Balance in InP Quantum Dot Light-Emitting Diodes

*Dongbeom Heo, Jun Hyuk Chang, Doyoon Shin, Jeonghun Kwak, Wanki Bae, and Hyunho Lee**

Balanced charge injection into the emissive layer is a prerequisite for achieving highly efficient quantum dot light-emitting diodes (QLEDs). The similar energy distribution of charge transport layers and indium phosphide (InP) quantum dots (QDs) facilitates excess electron injection to the InP QD layer. In this study, magnesium-doped ZnO nanoparticles (ZMO NPs) are modified to suppress the electron injection to the InP QD layer. Particularly, hydroxyl groups are effectively replaced by electrically stable states through the passivation of ZMO NPs, retarding electron injection through the ZMO NP layer. The modified ZMO-NP-based InP QLEDs exhibit a maximum external quantum efficiency of 9.6% with a substantially enhanced operational lifetime compared with that of devices made with unmodified ZMO NPs.

1. Introduction

Quantum dot light-emitting diodes (QLEDs) have been widely studied because of the superior optoelectronic characteristics of quantum dots (QD).[1–9] The tunable size of QDs enables the precise control of the energy bandgap, providing color emissions throughout the visible range.[10–13] QLEDs exhibit high color purities and satisfy the REC2020 standard.[14] Full color (red, green, blue) patterning for depositing the QD layer is available via solution-based manufacturing processes such as transfer and ink-jet printing.[15–18] Given these advantages, QLEDs are being considered as next-generation light sources for various display applications.

D. Heo, H. Lee
Department of Electronic Engineering
Kwangwoon University
Seoul 01897, Republic of Korea
E-mail: hyunho@kw.ac.kr

J. H. Chang, D. Shin, W. Bae
SKKU Advanced Institute of Nano Technology and Department of Nano Engineering
Sungkyunkwan University
Suwon 16419, Republic of Korea

J. Kwak
Department of Electrical and Computer Engineering
Inter-University Semiconductor Research Center
Seoul National University
Seoul 08826, Republic of Korea

The ORCID identification number(s) for the author(s) of this article can be found under https://doi.org/10.1002/adom.202202256.

DOI: 10.1002/adom.202202256

An efficient radiative recombination process in the emission layer is required to develop efficient QLEDs. Further, there are several possible loss mechanisms in QLEDs. Interfacial trap states in charge transporting layers (CTLs),[19–21] defect sites on QDs,[22–25] and charge injection imbalance[7,26] can reduce QLED performance. Non-radiative Auger recombination is considered the primary loss mechanism, which is caused by excess charge injection to QDs.[23,27–29] Efficient and balanced charge injection into the QD emission layer is needed to achieve radiative recombination without severe loss mechanisms. The energy level distribution between the QD and adjacent CTL is critical because larger energy gaps significantly impede the charge transport between layers. QDs produced for light-emission applications have energy bands that are located at deeper sites (valence band level approximately 6.5 eV) compared to those of commercially available CTLs.[23] Hole injection from a hole transport layer (HTL) to an emission layer (EML) has been widely reported to be inefficient owing to energetic misalignment.[30–32] Enhancing hole injection into emissive QDs was proposed as the key parameter for balancing charge injection; specifically, this was performed via HTL doping to achieve hole mobility or a double HTL structure for gradient hole injection.[33,34] Balanced charge injection can be achieved by inhibiting electron injection from the electron transport layer (ETL) to the EML. The insertion of an electron injection inhibitor such as poly(methyl methacrylate) (PMMA) at the ETL/EML interface has been shown to suppress the excess electron injection to the QD layer.[7] The ETL can be doped to achieve a lower electron mobility.[35]

Zinc oxide (ZnO) nanoparticles (NPs) have been commonly used as an ETL.[4,9,36,37] NPs have facile synthesis processes and stable electrochemical characteristics that are favorable features for electrical applications in optoelectronic devices.[5,38] The conduction band minimum (CBM) of ZnO NPs is similar to that of QDs, which leads to excessive injection of electrons into the QD layer.[26] The excess electron injection can induce nonradiative (Auger) recombination in the emission layer that reduces the device performance and operational stability of QLEDs.[26,39] Mg doping of ZnO has been widely reported to lower the electron mobility in ZnO NP and to suppress the electron injection through the ZnO NP ETL. Notably, Mg-doped ZnO (ZMO) exhibited a decrease in the mobility when the doping concentration of Mg was varied.[40] An

upshift of the CBM was observed when the Mg doping ratio was increased further, inhibiting electron injection to the QD layer.[41] However, the inherent optical quenching that occurs at the surface of ZMO can inhibit the performance of LEDs.[40] The common terminating groups on the ZnO surface (O—H or H—O—H bonds) are strong exciton quenching sites that diminish the luminance of QDs, especially at the QD/ZMO interface.[40,42] Additional steps for restoring optoelectrical quenching sites are required to passivate the hydroxyl groups on the surface of the ZMO NPs.

In this study, we effectively suppressed optoelectrical quenching sites on the surface of ZMO NPs by adopting an additional passivation step during the synthesis process. Mixed passivation solvents, namely hexane and isopropyl alcohol (IPA), manipulated the oxygen sites in ZMO, resulting in enhanced emissive performances with low leakage currents in the indium phosphide (InP) QLEDs. The novel passivation agent by mixing solvents was introduced to utilize their functional effect on the nanoparticles such as carbon chain removal (hexane) and diluting hydroxyl groups (IPA).[43,44] A maximum external quantum efficiency (EQE) of approximately 9.6% was exhibited by the InP QLED with the modified ZMO NPs, which is a 1.3-fold enhancement from the EQE of the control device (7.2%). The modified device showed 8.5 h of operational lifetime (initial luminance (L_0) = 150 cd m^{-2}, lifetime to 70% of its initial luminance (LT_{70})), exhibiting significant enhancement from the lifetime (28 min, L_0 = 160 cd m^{-2}, LT_{70}) of the control device.

2. Results and Discussion

ZMO NPs were modified by introducing an additional passivation step during the synthesis process. A mixed solvent of hexane and IPA (volume ratio 4:1) was used during the purification process; full details of the methods are presented in the experimental section. **Figure 1**a,b shows transmission electron microscope (TEM) images of the control-ZMO NP (C-ZMO) and modified-ZMO (M-ZMO) NPs. The interplanar spacing of the crystal lattice that corresponds to the (101) lattice plane was measured as approximately 0.24 nm for both ZMO NPs. Figure 1c shows the X-ray diffraction (XRD) patterns of C-ZMO and M-ZMO, where each marked peak is assigned to the typical hexagonal wurtzite structure (JCPDS card no. 36-1451). No measurable peak shifts or change in the full-width half maximum (FWHM) broadening was observed in the M-ZMO XRD data compared with the C-ZMO result. Figure 1d,e shows selected area electron diffraction (SAED) patterns of ZMO NPs displaying the crystalline characteristics of ZMO. The same seven distinct planes of ZMO observed by XRD can be characterized ((100), (002), (101), (102), (110), (103), and (200)) by SAED and assigned based on the d-spacing distance from the center. The crystallite and grain sizes of the synthesized ZMO NPs were calculated (**Table 1**) by utilizing the d-spacing parameters measured from the XRD and SAED patterns. The grain size was calculated by Equation (1).

$$\text{Grain size} = 0.9 \times \lambda \div (\text{FWHM} \times \cos\theta) \quad (1)$$

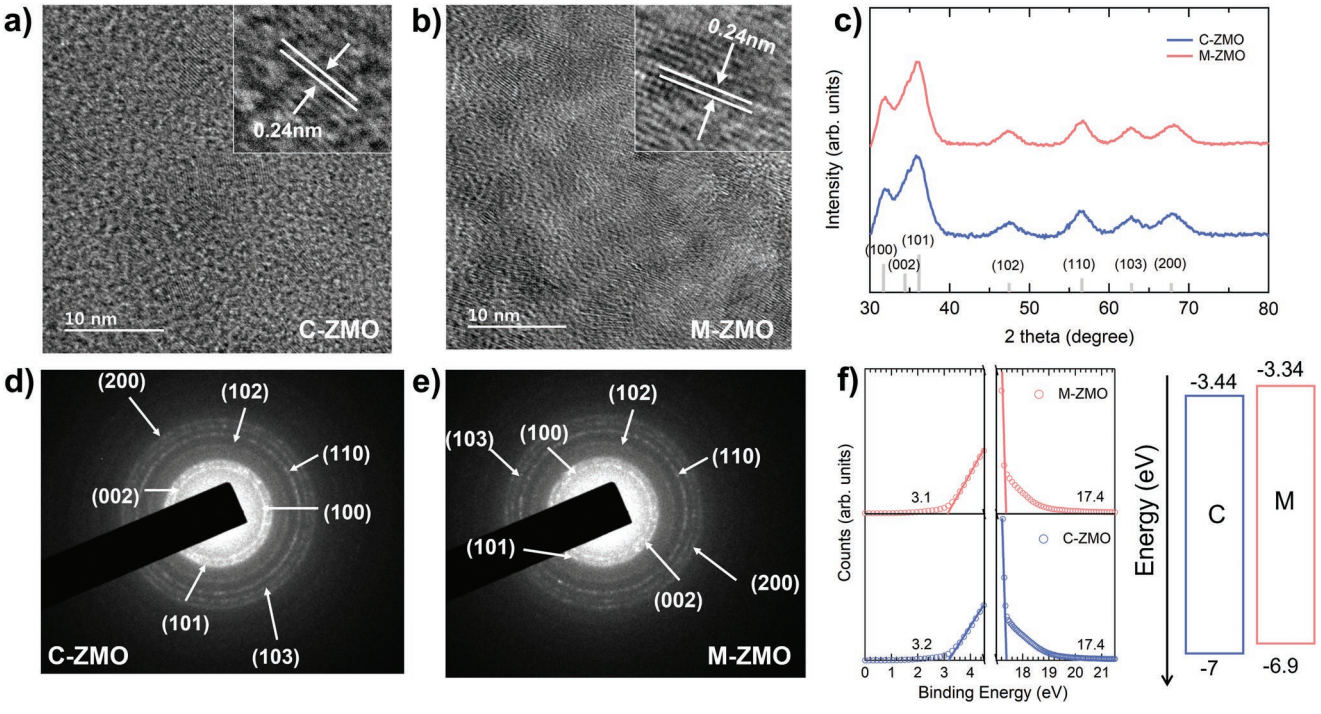

Figure 1. TEM images of a) C-ZMO and b) M-ZMO. The inset on the right-top represents the magnified TEM images to show the interplanar d-spacings. c) XRD patterns of C-ZMO (blue) and M-ZMO (red) powders. Reference peaks from JCPDS card no. 36-1451 are shown as gray bars. SAED pattern of d) C-ZMO and e) M-ZMO. f) UPS of C-ZMO (blue) and M-ZMO (red) film on a glass substrate with the measured energy level diagram for C-ZMO (blue) and M-ZMO (red).

Table 1. Calculated values from the XRD data of C-ZMO and M-ZMO.

	Crystallite size [Å]	Bragg's angle at (1 0 1) planes ($2\theta^{\circ}$)	Grain size (D) [nm]	FWHM [°]	Inter planar spacing (d_{101}) [nm]
C-ZMO	40.2	36.0	6.6	2.2	2.5
M-ZMO	41.3	36.0	6.6	2.2	2.5

where λ is the wavelength of the incident X-ray, FWHM is the full width at half maximum of Bragg's angle at the (101) plane, and θ is the half value of Bragg's angle at the (101) plane, giving a grain size of 6.61 nm for both ZMO NPs. This suggests that the ZMO NP modification caused by introducing the hexane–IPA mixed solvent did not affect the formation of the physical structure of ZMO. The identical physical structure features observed imply that the morphological characteristics of both ZMO NP films in the devices are the same. The energetic distribution of both ZMO NPs was investigated by ultraviolet photoelectron spectroscopy (UPS) measurement and a Tauc plot (Figure 1f and Figure S1, Supporting Information). The cut-off energy for both ZMO NPs was measured to be 17.4 eV. The on-set energy was measured for C-ZMO and M-ZMO as 3.2 and 3.1 eV, respectively. The Tauc plot (Figure S1, Supporting Information) shows that the measured energy bandgap of both ZMO NPs was identical at 3.58 eV. The calculated energy levels of both ZMO NPs are displayed in Figure 1f. The conduction bands of each ZMO are in a minor gap that can be considered a similar state. This suggests that the Schottky barrier at the QD/ZMO NP interface would be unchanged between C-ZMO and M-ZMO, resulting in a minimal difference in electron injection rate caused by the energetic distribution.

The chemical structure of ZMO NPs was investigated by Fourier transform infrared (FTIR) as shown in **Figure 2**a. The spectral peaks in the range 1400–1600 cm^{-1} (OH bending) and 3000–3600 cm^{-1} (OH stretching) present the functional bonding of the hydroxyl group in ZMO.[45–46] The hydroxyl groups quench excitons, which suppress radiative recombination at the interface of the emission layer.[42] M-ZMO exhibited a significant decrease in absorbance at the hydroxyl group (wavenumber 1400–1600 cm^{-1} and 3000–3600 cm^{-1}) compared with C-ZMO, which implies that the chemical structure related to the oxide was modified through the passivation step. The decrease in O—H bending and stretching indicates that the luminance quenching spots were effectively passivated by the ZMO modification steps. This suggests that the M-ZMO ETL is expected to suppress the nonradiative recombination in the LEDs.

A different volume mixing ratio of IPA and hexane (1:1) was used to verify the effect of the IPA on the surface passivation. The effect of IPA passivation could not be investigated alone as it disperses nanoparticles during the precipitation step. Figure S2 (Supporting Information) shows FTIR of M-ZMO passivated with only hexane as the solvent resulting in an increased amount of hydroxyl groups on the surface of nanoparticles. The use of the 1:1 mixed solvent (hexane and IPA) exhibited an effective decrease in the amount of hydroxyl terminating groups. Therefore, we speculate that IPA alone would effectively target and detach hydroxyl groups on the surface of ZMO NPs.

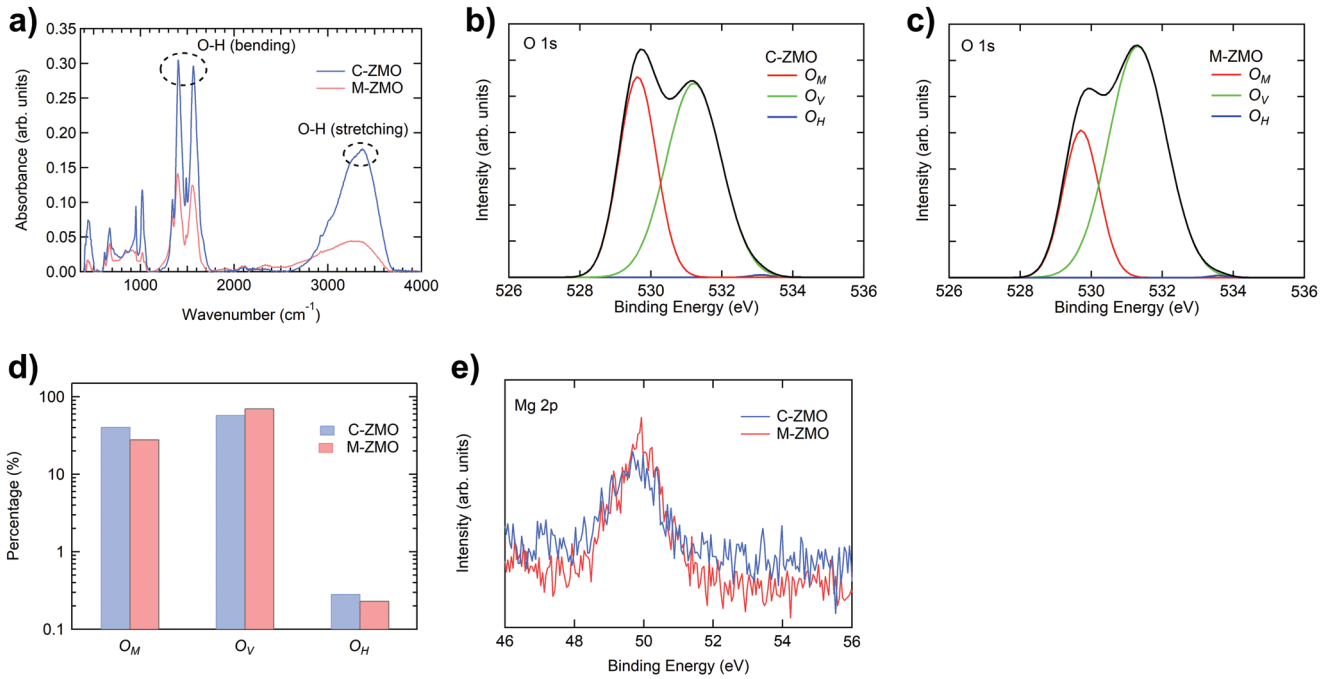

Figure 2. a) FTIR spectrum of C-ZMO (blue) and M-ZMO (red). XPS O 1s deconvolution of b) C-ZMO and c) M-ZMO film. The O_M, O_V, and O_H bonds are shown with red, green, and blue lines, respectively. (d) The atomic percentage of each oxygen bonding state for C-ZMO (blue) and M-ZMO (red) films. e) An XPS Mg 2p spectra of C-ZMO (blue) and M-ZMO (red) films.

The observed variation of the hydroxyl group in ZMO NPs by FTIR (Figure 2a) suggests that investigation into the oxygen bonding in the chemical structure of ZMO NPs is required. Figure 2b,c shows the X-ray photoelectron spectroscopy (XPS) from the O 1s bonding of the C-ZMO and M-ZMO, respectively. The optoelectrical characteristics of ZMO NPs are significantly affected by oxygen bonding, which consists of metal-oxygen (O_M), oxygen vacancy (O_V), and hydroxyl bonds (O_H).[40,47] The presence of each type of oxygen bonding can be calculated as a percentage of the distribution by deconvolution of the gaussian peak shapes from the O 1s curves for both ZMO NPs (Figure 2d). The O_M, O_V, and O_H levels are centered at 529.7, 531.3, and 533.3 eV, respectively. The atomic percentage of O_V for M-ZMO increased from 58.7% to 71.4%. The O_V has been reported to trap electrons, causing an increase in the electrical resistivity of ZMO NP films.[47] The electron injection from the ZMO NP film to the QD layer would be retarded because of increased oxygen vacancies. The atomic percentage decrease of O_H (from 0.29% to 0.23%) for M-ZMO is consistent with the decrease observed in the amount of hydroxyl group shown in FTIR when ZMO NPs are modified (Figure 2a). This suggests that ZMO NP modification can retard electron injection into QDs, suppressing luminance quenching. Figure S3a (Supporting Information) shows the XPS data from M-ZMO passivated with hexane solely indicating an increase in O_V (58.7 to 70.1%) similar to the change observed with the 4:1 mixed solvent passivation in Figure 2c. The atomic percentage of O_H was increased significantly to 4.3% with solely hexane, suggesting that the surface passivation with hexane effectively induces oxygen vacancies on the surface of ZMO NPs and introduces considerable quenching sites. Figure S3b (Supporting Information) shows XPS data from M-ZMO passivated with hexane and IPA in a 1:1 ratio. The use of IPA decreased the atomic percentage of O_H (4.3% to 1.7%) compared to passivation with solely hexane, while the atomic percentage of O_V remains in the same range. This supports the FTIR results (Figure 2a) that the surface passivation with IPA could remove hydroxyl groups on the surface of ZMO NPs. We further checked the effect of the IPA on the ZMO NP surface. Figure S4 (Supporting Information) shows XPS data from ZMO NP film and IPA washed ZMO NP film. After the ZMO NP film washed by IPA, the intensity of O_H bonds was decreased by half while O_M, O_V bonds remain in the similar range. Therefore, hydroxyl groups on the ZMO NP surfaces would be effectively removed because of the reaction between IPA and ZMP NP surfaces. The proposed chemical reaction between IPA and hydroxyl groups is shown in Figure S5 (Supporting Information). The effect of the passivation step on the atomic concentration of Mg has been measured by considering the Mg 2p bonding of C-ZMO and M-ZMO (Figure 2e) as it has been reported that the atomic concentration of Mg doping of ZnO NPs affects the electrical resistivity of the film.[40] No peak shifts or changes were observed in the Mg bonding for M-ZMO compared with C-ZMO. The intensity of Mg 2p has been shown to change significantly when the atomic ratio of Mg in ZMO varies during synthesis.[40] This suggests that the ZMO NP passivation step has not significantly changed the Mg chemical composition on the oxygen surface of the ZMO NPs.

Figure 3a shows the device structure of the QLEDs produced. The thickness of each layer was measured using a cross-sectional TEM image of the device (Figure 3b) showing

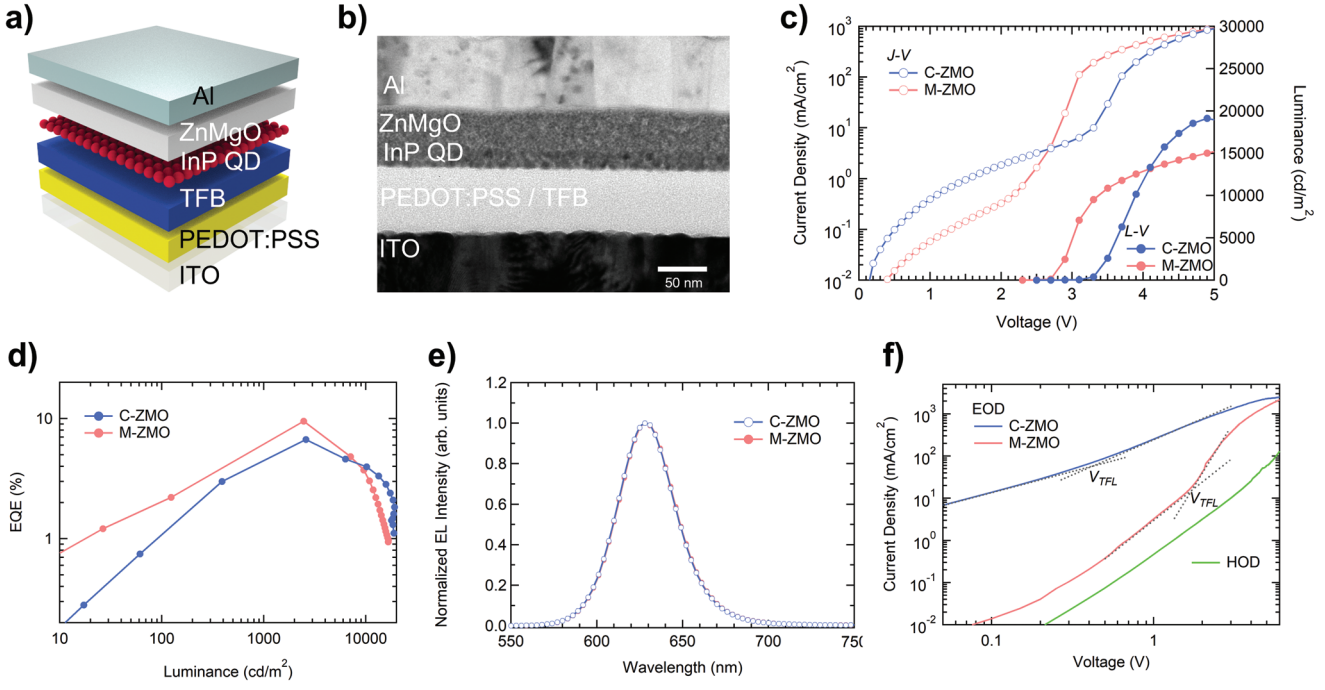

Figure 3. a) Schematic of the device structure. b) A cross-TEM image of the InP QLED. c) *J–V–L* characteristics of C-ZMO (blue) and M-ZMO (red) based devices. d) EQE of C-ZMO (blue) and M-ZMO (red) based devices with respect to luminance. e) Electroluminescence (EL) spectra of C-ZMO (blue) and M-ZMO (red) based devices. f) *J–V* characteristics of EOD for C-ZMO (blue) and M-ZMO (red) based devices and HOD (green).

Table 2. Emission characteristics of C-ZMO and M-ZMO based InP QLEDs.

	Turn-on voltage [V]	Max. current efficiency [cd A^{-1}]	Max. EQE [%]	Max. power efficiency [lm W^{-1}]	Peak wavelength [nm]	FWHM [nm]
C-ZMO	2.3	9.5	7.2	3.2	628	39
M-ZMO	2.3	12.9	9.6	4.5	628	39

the constituent layers: Indium tin oxide (ITO) (150 nm)/poly(3,4-ethylenedioxythiophene)-poly(styrenesulfonate) (PEDOT:PSS) (45 nm)/poly[(9,9-dioctylfluorenyl-2,7-diyl)-co-(4,4′-(N-(4-sec-butylphenyl)diphenylamine)] (TFB) (15 nm)/InP QD (20 nm)/ZMO NP (40 nm)/Al (100 nm). The 10 nm diameter InP QDs exhibit a photoluminescence quantum yield (PLQY) of 80%, as shown in Figure S6 (Supporting Information). Figure 3c shows the current density–voltage–luminance (*J–V–L*) curve of the devices, with blue and red lines representing the performance of the C-ZMO- and M-ZMO-based devices, respectively. A significant decrease in the current density level at the turn-on voltage and low-voltage regime (under 2.5 *V*) was observed when the ZMO NP was modified with the passivation solvents. The enhanced diode-characteristic (*J–V*) exhibits improved charge injection balance to the QD layer. The luminance increased significantly from 61 to 7079 cd m^{-2} at 3.1 V due to the modification in M-ZMO. The external quantum efficiency (EQE) of the devices is shown in Figure 3d, illustrating that the M-ZMO based devices had a maximum EQE of approximately 9.6% and the control device showed maximum EQE of approximately 7.2%. The statistical distribution of the EQE for each ZMO-NP-based device is shown in Figure S7 (Supporting Information). Figure 3e shows a pure red-colored emission (peak wavelength 628 nm, FWHM 39 nm) from both ZMO NP-based devices. The detailed emission profiles of the devices are summarized in **Table 2**. The enhancement in the luminance and reduction in the leakage currents gives the improvement in the efficiency of the M-ZMO based QLEDs compared with the C-ZMO. The enhanced luminance is representative of the optoelectrical quenching sites being effectively passivated by reducing the hydroxyl bonding on the ZMO NPs, in accordance with the results from the FTIR and XPS data (Figure 2). The downshift of the current level in the M-ZMO based device is caused by the increase in the atomic percent of O_V that directly suppresses electron injection to the QDs.

The electrical characteristics of ZMO NPs were investigated with single-carrier devices (Figure 3f). The blue and red lines represent the *J–V* curve of an electron-only device (EOD) based on C-ZMO and M-ZMO, respectively. The green line represents the *J–V* curve of a hole-only device (HOD). The structure of the EOD is ITO (150 nm)/ZMO NP (30 nm)/InP QD (20 nm)/ ZMO NP (30 nm)/Al (100 nm), which suggests that the *J–V* curve represents the electronic-transport characteristics of the device based on the electrical conductivity of the ZMO NPs or electron injection from the ZMO NPs to QDs. The HOD is composed of ITO (150 nm)/PEDOT:PSS (30 nm)/TFB (25 nm)/InP QD (20 nm) MoO_3 (10 nm)/Al (100 nm), representing the hole-transport characteristic through the device. The optimal radiative recombination in QLEDs is achieved by balancing the charge injection into the InP QD layer. An ideal *J–V* curve distribution for the EOD and HOD to illustrate a balanced carrier injection would be partially overlapping or closely located current levels.[48] The *J–V* curve of the M-ZMO-based EOD shows a significantly lower current level compared to that of the C-ZMO-based EOD. The downshift of the current level because of the ZMO modification is consistent with the trend of the *J–V* characteristic of QLEDs, as shown in Figure 3c, which illustrates a decrease in the electron transport characteristics of the M-ZMO film compared with C-ZMO. In the M-ZMO film, the atomic-percentage increment of O_V corresponds to an increase in the oxygen vacancies in the ZMO (as shown by the XPS spectra in Figure 2), enhancing the resistivity of the film by trapping electrons in the oxygen vacancies. Considering the oxygen vacancies with electron trap sites means the trap densities can be evaluated by the trap-filled limit voltage (V_{TFL}).[49,50] V_{TFL} is determined as the voltage at which there is an abrupt change (kink point) in the current injection. An exponential growth of the current at V_{TFL} indicates that the trap-filling process dominates the charge transport, which results in $J \propto V^{2-100}$ in the trap-filled limited region. The trap density can be calculated from V_{TFL} and is given by $n_t = \frac{2\varepsilon_r \varepsilon_0 V_{TFL}}{eL^2}$ where n_t is the trap density, ε_r is the relative dielectric constant of InP ($\varepsilon_r = 12.4$),[51,52] ε_0 is the vacuum permittivity, *e* is the elementary charge of an electron, and *L* is the InP QD film thickness. The V_{TFL} for C-ZMO- and M-ZMO-based devices were measured as approximately 0.4 and 1.7 V, respectively. The electron trap density of the C-ZMO- and M-ZMO-based devices was 1.37×10^{18} cm^{-3} and 5.83×10^{18} cm^{-3}, respectively. This suggests that the ZMO NP passivation process has created effective electron capturing sites by increasing the number of oxygen vacancies, thereby suppressing the electron injection process through the ZMO NP films. The *J–V* curves for M-ZMO-based EOD and HOD were similar owing to the effective electron capturing that provides optimized charge injection in the QLED operation.

Figure 4 shows the photoluminescence (PL) characteristics of C-ZMO and M-ZMO films with the steady-state PL displaying the enhanced PL intensity of InP QDs on M-ZMO film (Figure 4a). The measured reduction in hydroxyl bonding through the modification of ZMO NPs (as shown in Figure 2) suggests that the luminance quenching sites in M-ZMO are passivated. The enhancement of PL intensity reveals diminished exciton quenching at the interface of the emission layer and M-ZMO layer, which is consistent with the result of FTIR and XPS measurements. Figure 4b shows the transient dynamics of the PL with the blue and red data points representing the detected PL intensity points of InP QDs on C-ZMO and M-ZMO, respectively. The PL data points were fitted by a double-exponential function $y = a_1 \exp\left(\frac{-t_1}{\tau_1}\right) + a_2 \exp\left(\frac{-t_2}{\tau_2}\right)$, where the average PL lifetime was defined as $\tau_{ave} = \frac{a_1\tau_1^2 + a_2\tau_2^2}{a_1\tau_1 + a_2\tau_2}$. The detailed parameters of the fitted functions are summarized in **Table 3**. The average PL lifetime was calculated as 12.7 and

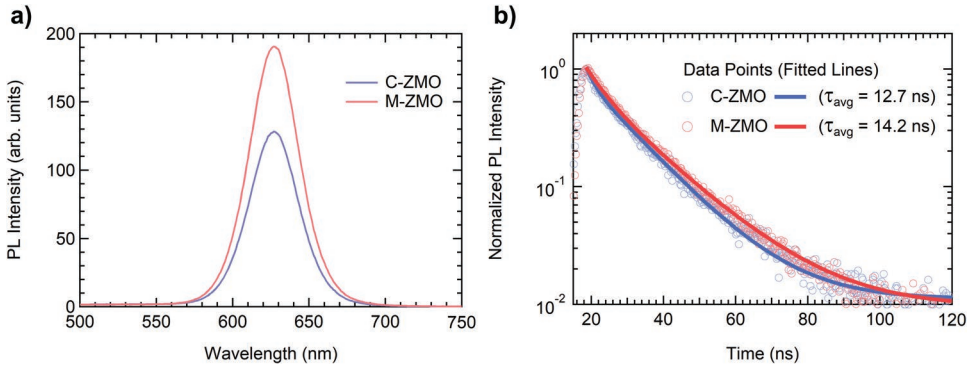

Figure 4. a) Steady-state PL spectra of the InP QD on C-ZMO (blue) and M-ZMO (red) film. b) Time-resolved PL of the InP QD on C-ZMO (blue) and M-ZMO (red) film. Solid lines represent double-exponential fitting lines.

14.2 ns for C-ZMO- and M-ZMO-based films, respectively. The increased PL lifetime indicates that superior radiative recombination processes in InP QD layer are achieved when the film is located next to a M-ZMO film rather than a C-ZMO film. This suggests that the enhanced light emission from M-ZMO-based QLEDs has been achieved by passivating optical quenching sites in ZMO NPs.

Figure 5 shows the operational lifetime of QLEDs. A constant voltage (2.45 and 2.3 V for C-ZMO and M-ZMO based devices to match the initial luminance around 150 cd m^{-2}, respectively) was applied for a luminance decay measurement. The L_0 for each device was measured as 160 and 150 cd m^{-2} for the C-ZMO and M-ZMO-based devices, respectively. LT_{70} lifetime was measured as approximately 28 and 502 min for the C-ZMO and M-ZMO based devices, respectively. The significant increase in operational lifetime of the M-ZMO device is due to the suppressed electron injection to the QD layer. The reduced excess electrons in the QD layer decrease the possibility of them participating nonradiative recombination such as Auger recombination.

3. Conclusion

We introduced a novel passivation step to the ZMO NP synthesis process. The purification steps using hexane and IPA mixed solvent (4:1 volume ratio) resulted in chemically modified surfaces of ZMO NPs. The amount of hydroxyl groups in ZMO NP was effectively reduced while the number of oxygen vacancies in ZMO NPs was increased. The oxygen vacancies in the M-ZMO provided effective electron traps that retarded electron injection to the QD layer by increasing the electron trap density. The matched charge injection balance into the QD layer produced a reduced current in the M-ZMO-based QLEDs in the low voltage regime ($V < 2.5$ V) compared with C-ZMO, resulting in efficient emissive characteristics (EQE: 9.6%, LT_{70}: 8.5 h). These consistent results on M-ZMO-based optoelectrical devices provide a production route for achieving charge injection balance in InP QLEDs.

Table 3. Transient PL coefficient extrapolation for InP QDs on C-ZMO and M-ZMO films.

	a_1	τ_1 [ns]	a_2	τ_2 [ns]
C-ZMO	0.26	2.2	0.74	13.3
M-ZMO	0.36	5.45	0.64	15.91

4. Experimental Section

Materials: Indium acetate ($In(Ac)_3$, 99.99%), zinc acetate ($Zn(Ac)_2$, 99.99%), 1-octadecene (ODE, 99%), oleic acid (OA, 99%), tris(trimethylsilyl)phosphine ($(TMS)_3P$, 99.9%), n-trioctylphosphine (TOP, 99%), selenium (Se, 99.9%), and sulfur (S, 99.9%) were purchased from Uniam. 1-dodecanethiol (DDT, ≥ 98%) and trioctylamine (TOA, 98%) were purchased from Sigma-Aldrich. PEDOT:PSS (AI4083) was purchased from Heraeus. Zinc acetate (Zn(Ac)2, >99.9%) and magnesium acetate tetrahydrate (Mg(Ac)2·4H2O, 99%) was purchased from Alfa Aesar. Tetramethylammonium hydroxide pentahydrate (TMAH, >97%), poly[(9,9-dioctylfluorenyl-2,7-diyl)-*co*-(4,4′-(*N*-(4-sec-butylphenyl) diphenylamine)] (TFB), ethanol, acetone, hexane, dimethyl sulfoxide (DMSO), isopropyl alcohol (IPA), and chlorobenzene (CB) were purchased from Sigma-Aldrich. All chemicals were used as received.

Synthesis of InP Core and InP/ZnSe/ZnS QDs: InP cores were prepared based on the previously reported method with minor modifications. All syntheses were carried out under an inert gas condition with the Schlenk line technique. 3 mmol of $In(Ac)_3$, 9 mmol of OA in 45 mL of ODE was degassed at 110 °C under vacuum for 2 h and backfilled with inert gas. 1.5 mmol of $(TMS)_3P$ diluted by 1 mL of TOP was injected into the reaction flask to form an indium-phosphine cluster. And the reaction

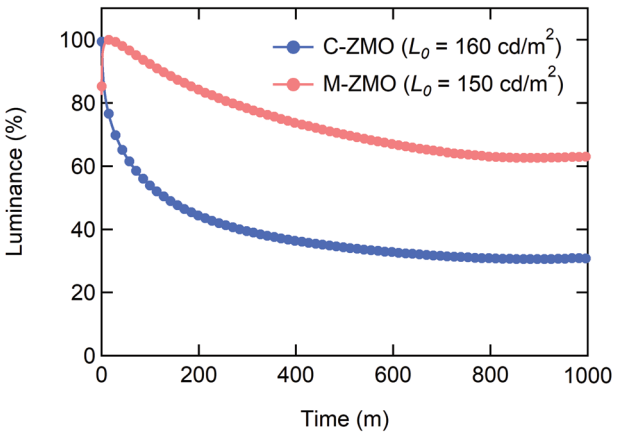

Figure 5. Luminance decay under constant voltage bias. Blue and red curves represent C-ZMO and M-ZMO based devices, respectively.

temperature was increased to 260 °C and maintained for 1 h to grow InP core. For further growth of InP core, the proper amount of indium and phosphine precursors were injected continuously. The synthesized InP core was purified via precipitation with ethanol and redispersion with toluene. Lastly, InP core was dispersed in 15 mL of toluene for further experiment.

InP/ZnSe/ZnS QDs were synthesized by using a previously synthesized InP core. 8 mmol of $Zn(Ac)_2$, 16 mmol of OA, and 30 mL of TOA were degassed under vacuum at 110 °C for 2 h and refilled with inert gas. And the reaction temperature was increased to 200 °C. At 200 °C, 1 mL of previously synthesized InP core was swiftly injected into the reaction flask. The reaction flask was then heated up to 340 °C. 4 mmol of TOPSe was injected to grow ZnSe shell. After 1 h, 2 mmol of TOPS was injected to grow ZnS shell. After 1 h of the reaction, the flask was cooled down to the room temperature. InP/ZnSe/ZnS QDs were purified via the precipitation/redispersion method.

Synthesis of ZMO NPs: ZMO NPs were synthesized using the precipitation-solution method. TMAH (1.36 g) was completely dissolved in ethanol (15 mL) at the atmosphere. And Zn acetate dihydrate (1.02 g) and Mg acetate tetrahydrate (7 wt%) was dissolved in DMSO (30 mL). 10 mL of TMAH solution was injected into Zn and Mg acetate solution at a rate of 480 mL h^{-1}. The mixed solution was stirred for 2 h 30 min. During the reaction, a nitrogen filled environment was maintained. Then, antisolvent (acetone) was poured into the mixed solution. The cloudy solution was stored overnight without any stirring. After being collected by centrifugation, the product was dried and dispersed in ethanol. For the passivation step to synthesize M-ZMO, the cloudy solution was stored 1 h without any stirring. The particle collection time related EL performances for C-ZMO and M-ZMO based devices are shown in Figure S8 (Supporting Information), respectively. After being collected by centrifugation, the product was dried and redispersed in acetone. The mixed solution of IPA and hexane (1:4 volume ratio) was added to the product in acetone. After being collected by centrifugation, the above purification step was carried out one more time. The supernatant solvents (acetone, hexane, and IPA) were discarded completely. The precipitated particles were dried in rough vacuum conditions. Finally, the precipitated product was dissolved in ethanol. All purification steps were processed in the glovebox.

Device Fabrication: The ITO-patterned glass was cleaned with acetone, IPA and deionized water. The dried substrates were further treated with UV-ozone for 15 min. PEDOT:PSS was spin-coated at 3000 rpm for 60 s, followed by annealing at 130 °C for 20 min in air. Then, the substrates were transferred to N_2 filled glove box (<0.1 ppm H_2O) for further fabrication. A 0.6 wt% solution of TFB dissolved in CB was spin-coated on the PEDOT:PSS layer at 4000 rpm for 30 s, followed by annealing at 150°C for 30 min. After cooling down to the room temperature, QD (InP/ZnSe/ZnS) in octane was spin-coated at 3000 rpm for 30 s, and the film was annealed at 70 °C for 30 min. A solution of desired ZMO NPs was spin-coated at 4000 rpm for 30 s and annealed at 70 °C for 30 min. Finally, Al cathode was thermally evaporated at a rate of 1≈2 A s^{-1} under 3×10^{-6} torr. The devices were encapsulated with cover glass.

Device Characterization: UV–vis absorption and visible photoluminescence (PL) spectra were collected with UV-1800 (Shimadzu), and Fluromax-4 spectrometer (Horiba Science). The current–voltage–luminance characteristics and EL spectra were measured by a CS-2000 spectroradiometer (Minolta) and a source meter (Keithley 2450). FTIR was recorded in diffuse reflectance mode by IFS66v/s & Hyperion3000 by Bruker. UPS was acquired using a helium excitation source by FC-XP10(He 21.2 eV). XPS was obtained using Versaprobe iii photoelectron spectrometer. The PL spectra were measured by using FluoTime 300 fluorescence spectrometer. SAED and HR-TEM were measured by JEM-2100F. XRD was measured with D8 Advance.

Supporting Information

Supporting Information is available from the Wiley Online Library or from the author.

Acknowledgements

This work was supported by the Basic Science Research Program (NRF-2022R1F1A1066526) through the National Research Foundation of the Ministry of Education, Republic of Korea. This research (for H.L.) was partially supported by Basic Science Research Program through the National Research Foundation of Korea (NRF) funded by the Ministry of Education (No. 2018R1A6A1A03025242).

Conflict of Interest

The authors declare no conflict of interest.

Data Availability Statement

The data that support the findings of this study are available from the corresponding author upon reasonable request.

Keywords

charge balance, InP, quantum dot light-emitting diodes, zinc magnesium oxide

Received: September 25, 2022
Revised: January 25, 2023
Published online:

[1] V. L. Colvin, M. C. Schlamp, A. P. Alivisatos, *Nature* **1994**, *370*, 354.
[2] A. P. Alivisatos, *Science* **1996**, *271*, 933.
[3] S. Coe, W.-K. Woo, M. Bawendi, V. Bulović, *Nature* **2002**, *420*, 800.
[4] J. Kwak, W. K. Bae, D. Lee, I. Park, J. Lim, M. Park, H. Cho, H. Woo, D. Y. Yoon, K. Char, S. Lee, C. Lee, *Nano Lett.* **2012**, *12*, 2362.
[5] J. Lim, Y.-S. Park, V. I. Klimov, *Nat. Mater.* **2018**, *17*, 42.
[6] T. Lee, B. J. Kim, H. Lee, D. Hahm, W. K. Bae, J. Lim, J. Kwak, *Adv. Mater.* **2022**, *34*, 2106276.
[7] X. Dai, Z. Zhang, Y. Jin, Y. Niu, H. Cao, X. Liang, L. Chen, J. Wang, X. Peng, *Nature* **2014**, *515*, 96.
[8] J. Lim, M. Park, W. K. Bae, D. Lee, S. Lee, C. Lee, K. Char, *ACS Nano* **2013**, *7*, 9019.
[9] Y.-H. Won, O. Cho, T. Kim, D.-Y. Chung, T. Kim, H. Chung, H. Jang, J. Lee, D. Kim, E. Jang, *Nature* **2019**, *575*, 634.
[10] C. B. Murray, D. J. Norris, M. G. Bawendi, *J. Am. Chem. Soc.* **1993**, *115*, 8706.
[11] F. Cao, S. Wang, F. Wang, Q. Wu, D. Zhao, X. Yang, *Chem. Mater.* **2018**, *30*, 8002.
[12] W. K. Bae, K. Char, H. Hur, S. Lee, *Chem. Mater.* **2008**, *20*, 531.
[13] W. K. Bae, M. K. Nam, K. Char, S. Lee, *Chem. Mater.* **2008**, *20*, 5307.
[14] R. Zhu, Z. Luo, H. Chen, Y. Dong, S.-T. Wu, *Opt. Express* **2015**, *23*, 23680.
[15] T.-H. Kim, K.-S. Cho, E. K. Lee, S. J. Lee, J. Chae, J. W. Kim, D. H. Kim, J.-Y. Kwon, G. Amaratunga, S. Y. Lee, B. L. Choi, Y. Kuk, J. M. Kim, K. Kim, *Nat. Photonics* **2011**, *5*, 176.
[16] H. Roh, D. Ko, D. Y. Shin, J. H. Chang, D. Hahm, W. K. Bae, C. Lee, J. Y. Kim, J. Kwak, *Adv. Opt. Mater.* **2021**, *9*, 2002129.
[17] M. Chen, L. Xie, C. Wei, Y.-Q.-Q. Yi, X. Chen, J. Yang, J. Zhuang, F. Li, W. Su, Z. Cui, *Nano Res.* **2021**, *14*, 4125.
[18] C. Xiang, L. Wu, Z. Lu, M. Li, Y. Wen, Y. Yang, W. Liu, T. Zhang, W. Cao, S.-W. Tsang, B. Shan, X. Yan, L. Qian, *Nat. Commun.* **2020**, *11*, 1646.

[19] J. H. Chang, P. Park, H. Jung, B. G. Jeong, D. Hahm, G. Nagamine, J. Ko, J. Cho, L. A. Padilha, D. C. Lee, C. Lee, K. Char, W. K. Bae, *ACS Nano* **2018**, *12*, 10231.
[20] F. Wang, Q. Hua, Q. Lin, F. Zhang, F. Chen, H. Zhang, X. Zhu, X. Xue, X. Xu, H. Shen, H. Zhang, W. Ji, *Adv. Opt. Mater.* **2022**, *10*, 2200319.
[21] M. Chrzanowski, G. Zatryb, P. Sitarek, A. Podhorodecki, *ACS Appl. Mater. Interfaces* **2021**, *13*, 20305.
[22] M. Nirmal, B. O. Dabbousi, M. G. Bawendi, J. J. Macklin, J. K. Trautman, T. D. Harris, L. E. Brus, *Nature* **1996**, *383*, 802.
[23] J. M. Pietryga, Y.-S. Park, J. Lim, A. F. Fidler, W. K. Bae, S. Brovelli, V. I. Klimov, *Chem. Rev.* **2016**, *116*, 10513.
[24] W. K. Bae, L. A. Padilha, Y.-S. Park, H. McDaniel, I. Robel, J. M. Pietryga, V. I. Klimov, *ACS Nano* **2013**, *7*, 3411.
[25] J. Lim, B. G. Jeong, M. Park, J. K. Kim, J. M. Pietryga, Y.-S. Park, V. I. Klimov, C. Lee, D. C. Lee, W. K. Bae, *Adv. Mater.* **2014**, *26*, 8034.
[26] W. K. Bae, Y.-S. Park, J. Lim, D. Lee, L. A. Padilha, H. McDaniel, I. Robel, C. Lee, J. M. Pietryga, V. I. Klimov, *Nat. Commun.* **2013**, *4*, 2661.
[27] Y.-S. Park, W. K. Bae, J. M. Pietryga, V. I. Klimov, *ACS Nano* **2014**, *8*, 7288.
[28] Y.-S. Park, W. K. Bae, L. A. Padilha, J. M. Pietryga, V. I. Klimov, *Nano Lett.* **2014**, *14*, 396.
[29] Y. Lee, D.-Y. Jo, T. Kim, J.-H. Jo, J. Park, H. Yang, D. Kim, *ACS Appl. Mater. Interfaces* **2022**, *14*, 12479.
[30] W. Wu, Z. Chen, Y. Zhan, B. Liu, W. Song, Y. Guo, J. Yan, X. Yang, Z. Zhou, W.-Y. Wong, *Adv. Mater. Interfaces* **2021**, *8*, 2100731.
[31] J. Chen, D. Song, S. Zhao, B. Qiao, W. Zheng, Z. Xu, *Org. Electron.* **2021**, *94*, 106169.
[32] Y. Fang, P. Bai, J. Li, B. Xiao, Y. Wang, Y. Wang, *ACS Appl. Mater. Interfaces* **2022**, *14*, 21263.
[33] N. Oh, B. H. Kim, S.-Y. Cho, S. Nam, S. P. Rogers, Y. Jiang, J. C. Flanagan, Y. Zhai, J.-H. Kim, J. Lee, Y. Yu, Y. K. Cho, G. Hur, J. Zhang, P. Trefonas, J. A. Rogers, M. Shim, *Science* **2017**, *355*, 616.
[34] Y. Yu, Y. Liang, J. Yong, T. Li, M. S. Hossain, Y. Liu, Y. Hu, K. Ganesan, E. Skafidas, *Adv. Funct. Mater.* **2022**, *32*, 2106387.
[35] Y. Lee, B. G. Jeong, H. Roh, J. Roh, J. Han, D. C. Lee, W. K. Bae, J.-Y. Kim, C. Lee, *Adv. Quantum Technol.* **2018**, *1*, 1700006.
[36] J. Pan, J. Chen, Q. Huang, Q. Khan, X. Liu, Z. Tao, Z. Zhang, W. Lei, A. Nathan, *ACS Photonics* **2016**, *3*, 215.
[37] W. Zhang, S. Ding, W. Zhuang, D. Wu, P. Liu, X. Qu, H. Liu, H. Yang, Z. Wu, K. Wang, X. W. Sun, *Adv. Funct. Mater.* **2020**, *30*, 2005303.
[38] P. Fan, D. Zhang, Y. Wu, J. Yu, T. P. Russell, *Adv. Funct. Mater.* **2020**, *30*, 2002932.
[39] J. Lim, Y.-S. Park, K. Wu, H. J. Yun, V. I. Klimov, *Nano Lett.* **2018**, *18*, 6645.
[40] M. Chrzanowski, M. Kuchowicz, R. Szukiewicz, P. Sitarek, J. Misiewicz, A. Podhorodecki, *Org. Electron.* **2020**, *80*, 105656.
[41] L. Wang, J. Pan, J. Qian, W. Lei, Y. Wu, W. Zhang, D. K. Goto, J. Chen, *J. Mater. Chem. C* **2018**, *6*, 8099.
[42] H.-M. Kim, D. Geng, J. Kim, E. Hwang, J. Jang, *ACS Appl. Mater. Interfaces* **2016**, *8*, 28727.
[43] J. Yang, D. Hahm, K. Kim, S. Rhee, M. Lee, S. Kim, J. H. Chang, H. W. Park, J. Lim, M. Lee, H. Kim, J. Bang, H. Ahn, J. H. Cho, J. Kwak, B. Kim, C. Lee, W. K. Bae, M. S. Kang, *Nat. Commun.* **2020**, *11*, 2874.
[44] J. Louis, N. T. Padmanabhan, M. K. Jayaraj, H. John, *Mater. Adv.* **2022**, *3*, 4322.
[45] G. Nagaraju, S. Udayabhanu, S. A. Prashanth, M. Shastri, K. V. Yathish, C. Anupama, D. Rangappa, *Mater. Res. Bull.* **2017**, *94*, 54.
[46] R. Wahab, S. G. Ansari, Y. S. Kim, H. K. Seo, G. S. Kim, G. Khang, H.-S. Shin, *Mater. Res. Bull.* **2007**, *42*, 1640.
[47] H.-M. Kim, S. Cho, J. Kim, H. Shin, J. Jang, *ACS Appl. Mater. Interfaces* **2018**, *10*, 24028.
[48] S.-K. Kim, H. Yang, Y.-S. Kim, *J. Appl. Phys.* **2019**, *126*, 185702.
[49] R. H. Bube, *J. Appl. Phys.* **1962**, *33*, 1733.
[50] L. Xu, J. Li, B. Cai, J. Song, F. Zhang, T. Fang, H. Zeng, *Nat. Commun.* **2020**, *11*, 3902.
[51] C. Hilsum, S. Fray, C. Smith, *Solid State Commun.* **1969**, *7*, 1057.
[52] L. G. Meiners, *J. Appl. Phys.* **1986**, *59*, 1611.